Inorganic Chemistry

Article

pubs.acs.org/IC

Lithium Storage Properties of a Bioinspired 2-Line Ferrihydrite: A Silicon-Doped, Nanometric, and Amorphous Iron Oxyhydroxide

Hideki Hashimoto,*[,†,‡] Yuta Nishiyama,[†] Masahiro Ukita,[†] Ryo Sakuma,[†] Makoto Nakanishi,[†] Tatsuo Fujii,[†] and Jun Takada[†,‡]

[†]Graduate School of Natural Science and Technology, Okayama University, Okayama 700-8530, Japan

[‡]JST, CREST, Okayama 700-8530, Japan

Supporting Information

ABSTRACT: Inspired by a nanometric iron-based oxide material of bacterial origin, silicon (Si)-doped iron oxyhydroxide nanoparticles or 2-line ferrihydrites (2Fhs) were prepared and their lithium (Li) storage properties were investigated. The structures of the Si-doped 2Fhs strongly depended on the Si molar ratio [x = Si/(Fe + Si)] whose long-range atomic ordering gradually vanished as the Si molar ratio increased, with a structural change from nanocrystalline to amorphous at x = 0.30. The most striking properties were observed for the sample with x = 0.30. Over the voltage range of 1.5−4.0 V at a current rate of 500 mA/g, this material exhibited a relatively high reversible capacity of ∼100 mAh/g, which was four times greater than that of the Si-free 2Fh and indicated a good rate capability and cyclability. The large capacity and good rate and cycle performances are presumably because of the amorphous structure and the strong and stabilizing covalent Si−O bonds, respectively. The minor amount of Si^{4+} in the structure of the iron oxyhydroxides is considered to improve the electrochemical properties. Use of more appropriate doping elements and fabrication of more appropriate nanostructures could drastically improve the Li storage properties of the developed bioinspired material.

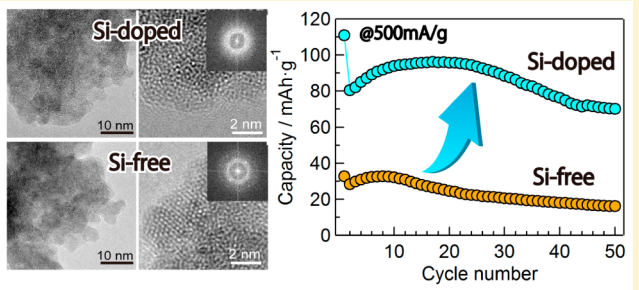

INTRODUCTION

Lithium (Li)-ion batteries exhibiting excellent rate capability and cyclability are strongly desired for use in electric vehicles, portable electric devices, and other applications. In recent times, a titanium oxide electrode material, $Li_4Ti_5O_{12}$, generating a 1.5 V class potential versus Li/Li^+ has attracted much attention as an anode material for applications requiring fast charge/discharge properties because of its high-rate capability and long-term cycle life.[1] Although this oxide material has an intrinsically poor electrical conductivity and low lithium diffusion coefficient, nanosizing of the particles greatly enhances the electrochemical lithium intercalation/deintercalation performance.[2,3] Nanosized iron oxides such as α-Fe_2O_3, γ-Fe_2O_3, Fe_3O_4, and α-FeOOH have the potential to exhibit capacities similar to that of $Li_4Ti_5O_{12}$, i.e., 100−300 mAh/g in the voltage range of 1.5−4.0 V.[4−11] Therefore, it would be quite meaningful for the battery industry if these extremely cost-effective and environmentally benign materials could serve as electrode materials for applications requiring fast charge/discharge performance. However, the cyclabilities and rate capabilities of simple iron oxides are intrinsically insufficient for practical applications.

We focused on a qualitatively different iron-based oxide naturally synthesized by a species of aquatic iron-oxidizing bacteria, *Leptothrix ochracea*.[12,13] The bacteriogenic oxide material is primarily composed of 3 nm diameter amorphous nanoparticles containing three metallic components, Fe^{3+}, Si^{4+}, and P^{5+}, mixed at an atomic ratio of 73:22:5.[14] Its X-ray diffraction pattern is similar to that of 2-line ferrihydrites (2Fhs), nanocrystalline iron oxyhydroxides.[15] Furthermore, the bacteriogenic material has a unique nano/microstructure, i.e., the nanoparticles assemble into microtubules of ∼1 μm in diameter.[14] Previously, we showed that the bacteriogenic material exhibited a reasonably good rate capability in the limited voltage range of 1.5−4.0 V; the discharge capacity exceeded 70 mAh/g at a very high current rate of 1670 mA/g.[16] The nanometric (particle size), compositional (coexistence of Si and P), and structural (amorphous) features of the bacteriogenic material most likely contribute to the very efficient in- and out-diffusion of Li ions. The presence of covalent and robust Si−O and P−O tetrahedra may also lead to the flexible response to repeated (de)lithiation. The performance of the bacteriogenic material as a high-capacity $Fe^{3+} \rightleftharpoons Fe^0$ conversion electrode material (∼900 mAh/g) at voltages in the range of 0−3 V was also investigated.[14] Interestingly, the original atomically homogeneous material was completely converted during the first discharge process to a double-component composite, in which ∼2 nm diameter α-Fe-like particles are embedded in an amorphous Si− and P−oxide

Received: May 27, 2015
Published: July 14, 2015

DOI: 10.1021/acs.inorgchem.5b01165
Inorg. Chem. 2015, 54, 7593−7599

matrix accommodating Li ions. The excellent rate capability and cyclability appear to result from the architecture of the Fe-core/Si, P, (Li) matrix, which prevents the Fe cores from undesirable aggregation. Therefore, it is clear that the additional Si and P components play an extremely important role in the fast charge/discharge performance.

Herein, inspired by the bacteriogenic iron-based oxide material, we synthesized the Si-doped, nanometric, and amorphous iron oxyhydroxide. In particular, we systematically synthesized Si-doped nanometric iron oxyhydroxides or 2-line ferrihydrites (2Fhs) whose X-ray diffraction pattern is analogous to that of the bacteriogenic material.[15] The primary particle size of 2Fh is 1.5−3 nm in diameter,[17] and its crystallinity decreases by doping Si in the structure.[18] Therefore, the Si-doped 2Fh samples should be very close to the bacteriogenic material in terms of particle size and ionic structure. We investigated the electrochemical performance of synthesized Si-doped 2Fh samples in the limited voltage range of 1.5−4.0 V with the aim of using them as electrode materials for fast charge/discharge applications.

EXPERIMENTAL SECTION

Sample Preparation and Characterization. On the basis of previous reports, Si-doped samples were prepared as follows.[17,18] A 0.025 mol dm^{-3} aqueous $Fe(NO_3)_3{\cdot}9H_2O$ (Nacalai Tesque, 99.0%) solution and aqueous solutions of m-$Na_2SiO_3{\cdot}9H_2O$ (nacalai tesque) at appropriate concentrations were prepared. Then, the $Fe(NO_3)_3{\cdot}9H_2O$ solution was mixed with different m-$Na_2SiO_3{\cdot}9H_2O$ solutions to obtain final solutions, each with a volume of 1 dm^3. The Si concentration, x = Si/(Si + Fe), was adjusted such that x = 0−0.50 in 0.05 increments. Each solution was vigorously stirred during the slow addition of NH_3 aq (Nacalai Tesque, 28 wt %) until a pH of 10.0 was reached, and then stirring was continued for 15 min. Each obtained precipitate was repeatedly washed via centrifuging with distilled water until the electrical conductivity of the supernatant was below 10 μS/m and then vacuum dried and crushed to a powder using an alumina mortar. The crystallographic structures and microstructures of the samples were characterized using X-ray diffractometry (XRD; RINT-2000; Rigaku, Japan and BL04B2 at the SPring-8, Hyogo, Japan), transmission electron microscopy (TEM; JEM-2100F; JEOL, Japan), and scanning transmission electron microscopy (STEM; JEM-2100F with CEOS C_s-corrector; JEOL, Japan) in conjunction with electron energy-loss spectroscopy (EELS; GIF Tridiem; Gatan, Germany). Elemental analysis of each sample was performed via X-ray fluorescence spectroscopy (XRF; ZSX PrimusII; Rigaku, Japan), and the chemical binding states of the samples were determined using Fourier transform infrared spectroscopy (FTIR; Nicolet 6700; Thermo Scientific, USA).

Electrochemical Measurements. Half cells (2032 coin-type) were fabricated to evaluate the electrochemical performance of the samples. Assembly of the half-cells was performed in an Ar-filled glovebox. Lithium metal foil (Honjo Metal) was used as the counter electrode, and a 1 mol dm^{-3} $LiPF_6$ solution in a 3:7 v/v mixture of ethylene carbonate/diethyl carbonate (EC/DEC) (Tomiyama Chemicals) was employed as the electrolyte. A porous polypropylene film (Celgard 2400) was used as the separator. The working electrode comprised 85 wt % Si-doped 2Fh samples (x = 0, 0.15, 0.20, 0.30, 0.40, 0.50), 10 wt % electrical conducting material (7:3 mixture of KETJENBLACK ECP from Lion and vapor-grown carbon fiber (VGCF) from Showa Denko), and 5 wt % polyvinylidene fluoride (PVDF; Kureha) as the binder. The mixture was dissolved in n-methylpyrrolidone (NMP; Sigma-Aldrich) and spread on aluminum foil current collectors. Before addition of the PVDF and NMP, the Si-doped sample and electrical conducting material were mixed via ball milling (480 rpm, 4 h). The obtained sheets were dried at 120 °C in a vacuum overnight. Each sheet prepared with an Si-doped sample was then cut into a 16 mm ϕ disk and pressed onto aluminum mesh. Cell performance was evaluated using an electrochemical analyzer (BTS2004W-10; Nagano, Japan) under galvanostatic conditions in the voltage range of 1.5−4.0 V at 50 mA/g. The rate capability of the Si-doped sample with x = 0.30, which exhibited the best properties, was measured at current rates of 50, 100, 200, and 500 mA/g. The rate capability of a Si-free sample was also determined as a reference.

Ex-Situ Mössbauer Measurements. The paste for formation of the electrode was prepared by ball milling (400 rpm, 24 h, by zirconia ball) Si-free or Si-doped samples (x = 0.30; 70 wt %) and an electrical conducting material (10 wt %, 7:3 mixture of ECP and VGCF) and then adding a binder (20 wt %, polyethylenetetrafluoride (PTFE) from Du Pont-Mitsui Fluorochemicals) and an appropriate amount of ethyl alcohol. An electrode sheet was formed by rolling. Half-cells were assembled in an Ar-filled glovebox, and discharge/charge curves were measured using an electrochemical analyzer (Hokuto, SD-8) in the voltage range of 1.0−4.0 V at a current rate of 10 mA/g at 25 °C. After discharging at 1.54 and 1.0 V and charging at 4.0 V, the electrodes were removed in an Ar-filled groove box, washed with DME, and then encapsulated with polyimide film (12.5 μm, The Nilaco corporation). Then, Mössbauer spectra were collected at room temperature.

RESULTS AND DISCUSSION

Sample Preparation and Characterization. XRF analysis revealed that the actual Si molar ratios of the prepared Si-doped iron oxyhydroxide nanoparticles were lower than the loaded values. Thus, the values for samples with x = 0, 0.10, 0.20, 0.30, 0.40, and 0.50 were 0.074, 0.144, 0.213, 0.289, and 0.360, respectively (all data are listed in Table S1, Supporting Information). Hereafter, the sample names are labeled according to the loaded values. Two broad diffraction peaks near 2θ = 35° and 63° corresponding to the (11l) and (30l) planes of 2Fh, respectively, clearly indicated the formation of a monophasic 2Fh for all samples, as shown in XRD patterns of Figure 1a. These two peaks gradually broadened and shifted to lower angles as the Si molar ratio increased. Figure 1b shows the normalized total structure factors $S(Q)$ of the samples with x = 0, 0.10, 0.30, and 0.50. The X-ray scattering data collected at BL04B2 in SPring-8 (X-ray energy ≈ 61.46 keV) were corrected using a standard program for deriving the $S(Q)$ and the radial distribution functions (RDFs).[19] The strong scattering intensities observed in the small $S(Q)$ region for all samples suggest small particle sizes and/or porous features. Furthermore, while the diffraction profiles were similar for the samples with x = 0 and 0.10 and only slightly broadened for the sample with x = 0.30, a very broad diffraction profile with a bulge near Q = 1.5 $Å^{-1}$ was observed for the sample with x = 0.50, presumably indicating the formation of a network of SiO_4 tetrahedral units.[20] Figure 1c shows the RDFs derived from the Fourier transformation of the $S(Q)$ values seen in Figure 1b. The small peaks at 1.6 Å observed for the samples with x = 0.10, 0.30, and 0.50 correspond to the Si−O nearest neighbor correlation, and the peaks near 2.0 and 2.5−4.0 Å for all samples indicate the Fe−O nearest neighbor correlation and a mixture of various types of Fe−Fe correlations, respectively. The Si−O correlation intensified, the Fe−O correlation weakened, the Fe−Fe correlation peak profile changed, and the entire RDF profile broadened as the Si molar ratio increased. These diffraction results clearly indicate that the global connectivity of the SiO_4 and FeO_x polyhedral units in the 2Fh structure drastically changed because of Si doping. In particular, the crystallinity of the samples gradually decreased as the Si molar ratio increased. A detailed description of the atomic arrangement will be provided in the future.

Figure 2a shows FTIR spectra of 2Fh samples with x = 0, 0.10, 0.30, and 0.50. In the spectrum of the Si-free sample, the

DOI: 10.1021/acs.inorgchem.5b01165
Inorg. Chem. 2015, 54, 7593−7599

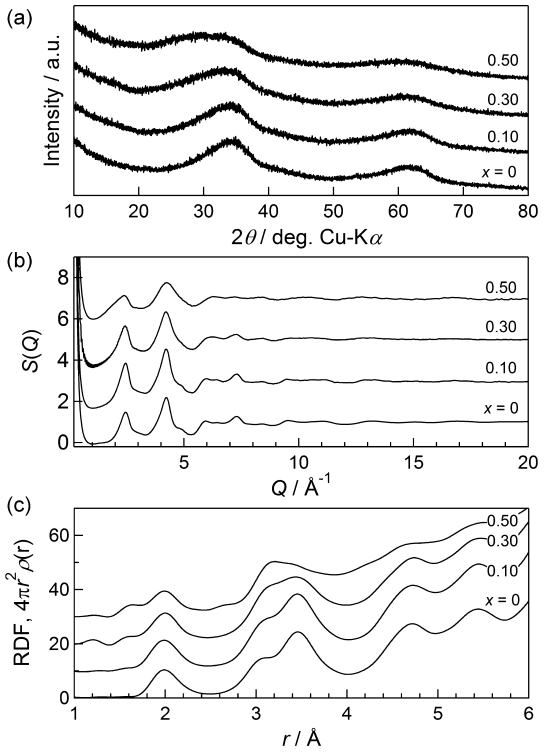

Figure 1. (a) XRD patterns of Si-doped iron oxyhydroxide nanoparticles with different Si molar ratios obtained using Cu Kα radiation. (b) Total structure factors $S(Q)$, and (c) RDFs of the samples. The crystallinity of the samples gradually decreased as the Si molar ratio increased.

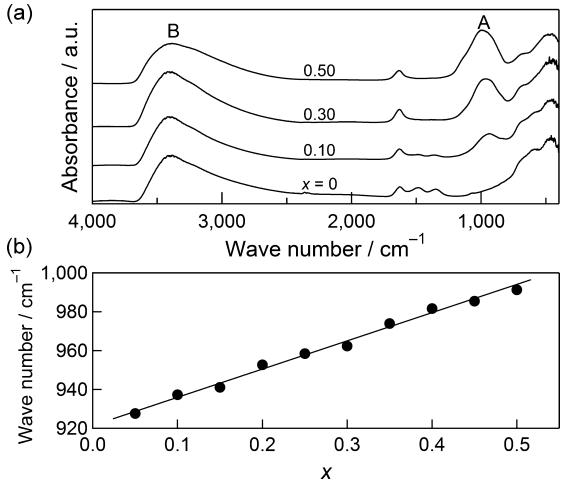

Figure 2. (a) FTIR spectra of Si-doped iron oxyhydroxide nanoparticles with different Si molar ratios. Bands A and B were assigned to Si−O−Fe and O−H stretching modes, respectively. (b) Variation of the wavenumber of band A as a function of the Si molar ratio. Band A shifted to higher wavenumbers as the Si molar ratio increased.

very broad band near 3400 cm^{-1}, which was assigned to the O−H stretching mode (labeled B),[21] was observed, suggesting the existence of OH groups and physisorbed water. This B band did not change as the Si molar ratio increased. On the other hand, in the spectra of the Si-doped samples, a band near 1000 cm^{-1}, which was assigned to the Si−O−Fe stretching mode (labeled A),[22,18] intensified and its position shifted to higher wavenumbers as the Si molar ratio increased. This wavenumber shift is plotted as a function of the Si molar ratio in Figure 2b. In general, the Si−O−Si stretching mode appears at ∼1100 cm^{-1}, and its position is known to shift to lower wavenumbers as the percentage of Si−O−Fe stretching modes increases.[18] The wavenumber shift for the Si−O−Fe stretching mode observed in the present study indicates the formation of Si−O−Fe bonds by Si doping, which is in good agreement with the results of Seehra et al.[18]

To investigate in detail the particle sizes, morphologies, microstructures, and elemental distributions of the Si-doped iron oxyhydroxide nanoparticles, high-resolution TEM (HRTEM) and STEM/EELS observations were performed. Figure 3 shows the micrographs of the samples. No distinctive morphology was observed for the samples, and they were found to comprise strongly aggregated nanoparticles. The average particle sizes were estimated using low-magnification TEM images (Figures 3a−d), and the values were constant and independent of the Si molar ratio with an average value for all samples of 3.4 nm (Figure 3e). This small particle size may be the origin of the strong scattering intensities in the small Q range seen in Figure 1b. Hexagonal plate-like particles were often observed in the samples with low Si molar ratios (e.g., Figures 3a, b, and f−h), and the edges became gradually rounder as the Si molar ratio increased (e.g., Figures 3c, d, and i−l). HRTEM images and their fast Fourier transformation (FFT) patterns are shown in Figure 3f−l. Although the HRTEM images for the samples with x = 0, 0.10, 0.20, and 0.25 were obscure, lattice fringes could be seen, and spots were detected in the corresponding FFT patterns (Figures 3f−i), which may plausibly indicate crystallinity and suggest that these samples were nanocrystalline materials. On the other hand, no clear lattice fringes and halo patterns were observed in the HRTEM images and FFT patterns, respectively, for the samples with x = 0.30, 0.40, and 0.50 (Figure 3j−l), indicating these samples were amorphous materials. High-angle annular dark field (HAADF)-STEM images of the samples with x = 0.30 and 0.50 are shown in Figure 3m and 3q, respectively. The Fe-K, Si-L, and O-K elemental maps acquired via STEM/EELS imaging are shown in Figure 3n−p (x = 0.3) and Figure 3r−t (x = 0.5). The obtained elemental maps clearly revealed that the Fe, Si, and O constituent elements were uniformly distributed throughout each sample structure at a resolution up to ∼1 nm.

Electrochemical Measurements. Figure 4a−f shows discharge/charge curves for the Si-doped iron oxyhydroxide nanoparticles with x = 0, 0.15, 0.20, 0.30, 0.40, and 0.50 in the voltage range of 1.5−4.0 V at a low current rate of 50 mA/g. All samples were able to intercalate and deintercalate Li ions reversibly, and their performance changed systematically depending on the Si molar ratio. Except for the Si-free sample, the changing point for the discharge curve gradient was observed at ∼1.6 V (Figures 4b−f), and the gradient became smaller and the discharge capacity was significantly extended beyond this point. Furthermore, the extended capacity below ∼1.6 V gradually decreased with repeating cycles, and eventually the changing point vanished, leading to a stable capacity. Lithium storage mechanisms before and after the changing point may differ from one another (see the discussion of the ex-situ Mössbauer analysis). Figure 4g displays the capacity retention data corresponding to the results shown in Figure 4a, 4c, and 4d−f for up to 20 cycles. The first discharge capacity of the Si-free sample was ∼140 mAh/g, and it faded to ∼90 mAh/g at 20 cycles. As the Si molar ratio increased, the first discharge capacity increased and reached a maximum value

DOI: 10.1021/acs.inorgchem.5b01165
Inorg. Chem. 2015, 54, 7593−7599

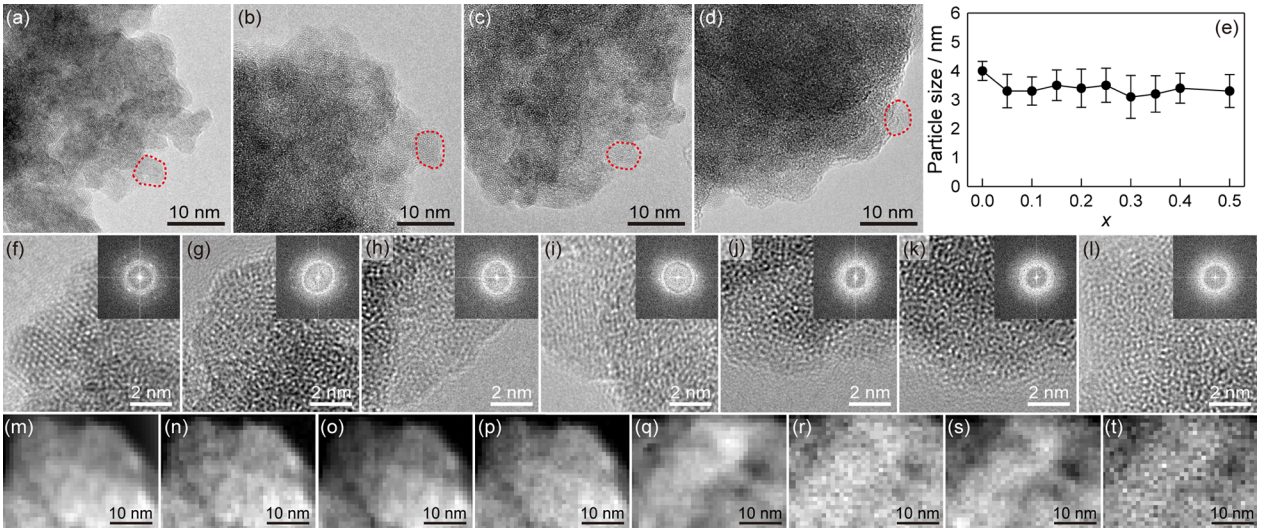

Figure 3. Electron micrographs of the samples. (a, b, c , and d) Low-magnification TEM images of the Si-doped iron oxyhydroxide nanoparticles with Si molar ratios x = 0, 0.20, 0.30, and 0.50, respectively. The moiety surrounded by dotted red line shows a primary particle. (e) Average particle sizes of the samples observed in the TEM images. (f, g, h, i, j, k, and l) High-resolution TEM images of the Si-doped iron oxyhydroxide nanoparticles with Si molar ratios x = 0, 0.10, 0.20, 0.25, 0.30, 0.40, and 0.50, respectively. Inset images correspond to the FFT patterns. (m) HAADF-STEM image of the sample with x = 0.30. (n, o, and p) Fe-K, Si-L, and O-K edge elemental maps, respectively, for the same area shown in m taken using STEM/EELS. (q) HAADF-STEM image of the sample with x = 0.50. (r, s, and t) Fe-K, Si-L, and O-K edge elemental maps, respectively, for the area shown in q taken using STEM/EELS. The electron probe was converged to ∼0.2 nm.

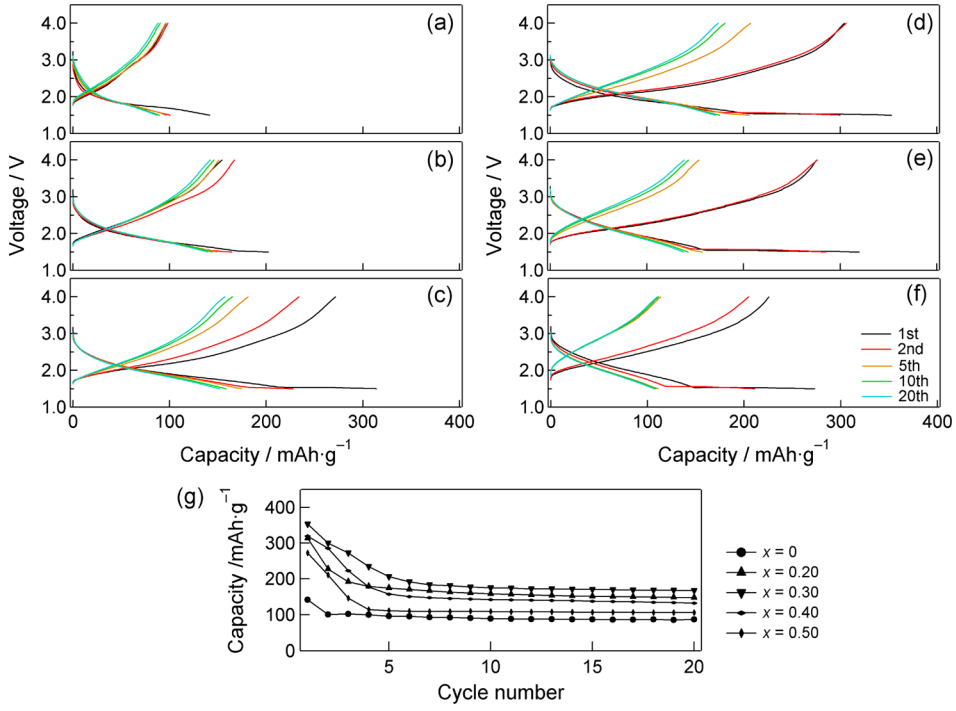

Figure 4. (a, b, c, d, e, and f) Discharge/charge curves of the Si-doped iron oxyhydroxide nanoparticles with Si molar ratios x = 0, 0.15, 0.20, 0.30, 0.40, and 0.50, respectively, in the voltage range of 1.5−4.0 V at a current rate of 50 mA/g. (g) Discharge capacity retention data for the samples.

of ∼350 mAh/g at x = 0.30, after which the capacity decreased to ∼270 mAh/g at x = 0.50. The reversible capacity at 20 cycles exhibited a similar trend. As the Si molar ratio increased, the 20th discharge capacity increased and reached a maximum value of ∼170 mAh/g at x = 0.30, after which it decreased to ∼110 mAh/g at x = 0.50. These results clearly revealed that Si doping of the 2Fh structure drastically increased the discharge capacity, with the highest reversible capacity for the sample with x = 0.30 twice that of the capacity for the Si-free sample. When the molar ratio of iron, which is the electrochemical center, decreases (i.e., the Si molar ratio increases in the present system), the discharge capacity is expected to decrease. The capacity decrease observed with the samples with $x \geq 0.4$ could be mainly due to this reason. However, such behavior was not observed with the samples with $x \leq 0.3$. Therefore, an appropriate quantity of Si doping is considered to intrinsically vary the structure of the 2Fh, resulting in the high capacity.

DOI: 10.1021/acs.inorgchem.5b01165
Inorg. Chem. 2015, 54, 7593−7599

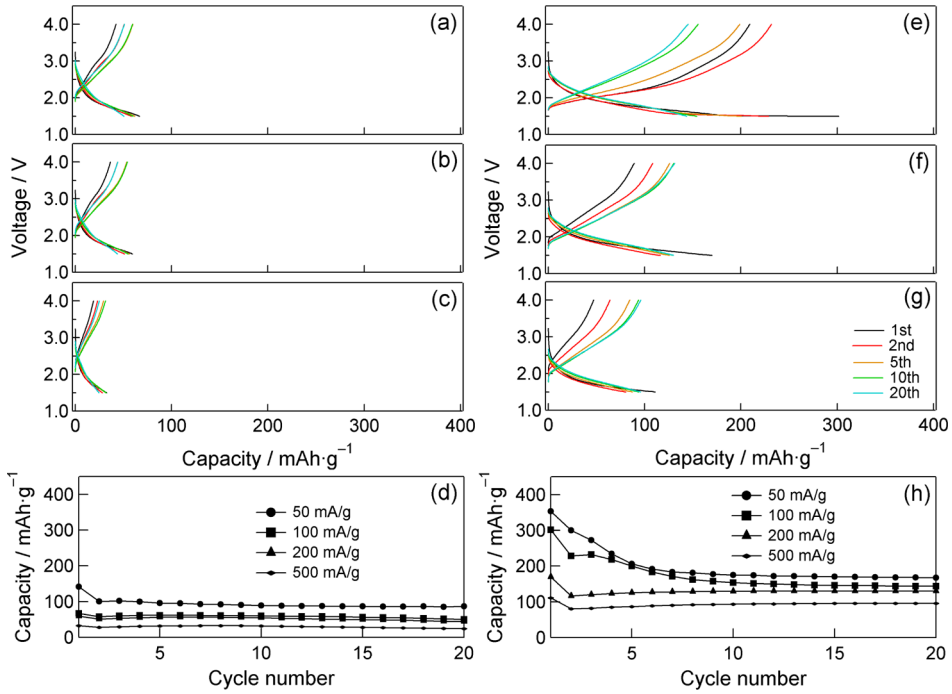

Figure 5. (a, b, and c) Discharge/charge curves of the Si-free iron oxyhydroxide sample in the voltage range of 1.5−4.0 V at current rates of 50, 200, and 500 mA/g, respectively. (d) Capacity retention data for the Si-free sample at various current rates. (e, f, and g) Discharge/charge curves of the Si-doped iron oxyhydroxide sample with x = 0.30 in the voltage range of 1.5−4.0 V at current rates of 50, 200, and 500 mA/g, respectively. (h) Capacity retention data for the sample with x = 0.30 at various current rates.

Next, the rate capability of the 2Fh with x = 0.30 was evaluated and compared to that of the Si-free sample. Discharge/charge curves at current rates of 100, 200, and 500 mA/g are shown in Figure 5a−c (Si-free) and 5e−g (x = 0.30). The capacity retention data at current rates of 50, 100, 200, and 500 mA/g are shown in Figure 5d (Si free) and 5h (x = 0.30). When the current rate was increased to 500 mA/g, the 20th discharge capacity of the Si-free sample decreased to ∼25 mAh/g. For the sample with x = 0.30, while the 20th discharge capacity also decreased as the current rate increased, a relatively high capacity of ∼100 mAh/g, which was four times greater than that of Si-free sample, was observed at the maximum current rate of 500 mA/g. This value is comparable to the capacity of the Si-free sample (∼90 mAh/g) at a current rate of 50 mA/g, suggesting that the sample with x = 0.30 can discharge/charge 10 times faster than Si-free sample. These results indicate that Si doping also improved the rate capability. However, it should be noted that although the sample with x = 0.30 displayed the best performance of the synthetic Si-doped iron oxyhydroxide nanoparticles, it did not reach the performance of the bacteriogenic iron-based oxide material, which exhibited ∼80 mAh/g at a current rate of 1670 mA/g.[16] Although the bacteriogenic material and the synthetic sample with x = 0.30 had nearly the same amorphous structure (atomic arrangement) and primary particle size, the aggregation state and morphology were completely different. The bacteriogenic material has ∼1 μm diameter tubule structures with mild aggregation of the primary particles, while the Si-doped sample had large agglomerates up to several tens of micrometers with strong aggregation of the primary particles. Such strong aggregation leads to inhibition of size reduction via ball milling and wetting with the electrolyte resulting in poorer performance than that of the bacteriogenic material. Thus, it is anticipated that the performance of the synthetic Si-doped materials can be improved by controlling the aggregation state through adjustment of the morphology and pore structure.

The performance of the Si-doped iron oxyhydroxide nanoparticle sample with x = 0.30 was then compared to that of conventional bare iron oxides. Reports suggest that α-Fe_2O_3 exhibits the 1st and 20th discharge capacities of 220 and 50 mAh/g, respectively, in the voltage range of 1.5−4.0 V at a current rate of 100 mA/g.[9] Furthermore, Fe_3O_4 has been reported to exhibit 1st and 30th discharge capacities of 130 and 100 mAh/g, respectively, at a current rate of 20 mA/g.[10] The sample with x = 0.30 exhibited 20th discharge capacities of 170 and 100 mA/g at current rates of 50 and 500 mA/g, respectively, indicating a rather high capacity and good rate capability compared to conventional α-Fe_2O_3 and Fe_3O_4. As has been reported by Hibino et al. for γ-Fe_2O_3 and acetylene black, intimate coating of powdered sample with an appropriate carbon material can drastically enhance the electrochemical performance of iron oxide.[11] Thus, further optimization of the electrode preparation process and carbon coating of the Si-doped samples prior to use could improve their electrochemical properties.

Ex-Situ Mössbauer Measurements. To investigate the valence state changes in the iron during discharge/charge measurement for the Si-doped iron oxyhydroxide nanoparticle sample with x = 0.30, ex-situ Mössbauer measurements were conducted (Figure 6). To obtain sufficient quantity of the sample for Mössbauer measurements, the electrode thickness was adjusted to ∼100 μm. As shown in Figure 6a, although the changing point for the discharge curve gradient appeared at a slightly lower voltage (1.54 V) than the discharge curves displayed in Figure 4d (∼1.6 V) because of the different electrode thickness, the entire discharge profiles were similar to those shown in Figure 4d. Mössbauer spectra before the run and when the sample was discharged at 1.54 and 1.0 V and

DOI: 10.1021/acs.inorgchem.5b01165
Inorg. Chem. 2015, 54, 7593−7599

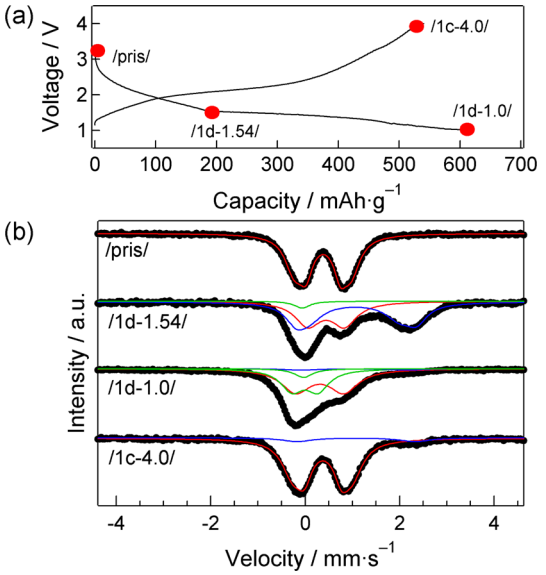

Figure 6. (a) First discharge/charge curves for the Si-doped iron oxyhydroxide sample with $x = 0.30$ in the voltage range of 1.0−4.0 V at a current rate of 10 mA/g used for ex-situ Mössbauer analysis. Data acquisition points are indicated by the red solid circles. (b) Mössbauer spectra of the pristine sample, samples discharged at 1.54 and 1.0 V, and samples charged at 4.0 V. Mössbauer parameters are listed in Table S2, Supporting Information.

charged at 4.0 V were acquired (Figure 6b and Table S2, Supporting Information). Prior to the run, the spectrum showed a single paramagnetic doublet with an isomer shift (*IS*) value of 0.36 mm/s, indicating that the sample contained trivalent iron (Figure 6b, /pris/). Upon discharge at 1.54 V, the spectrum included paramagnetic doublets for both Fe^{3+} and Fe^{2+} and paramagnetic singlet for Fe^0 (*IS* = 0.44, 0.98, and −0.07 mm/s, respectively) and the composition is a mixture of 41% Fe^{3+}, 55% Fe^{2+}, and 4% Fe^0, indicating that the reduction of Fe^{3+} to Fe^{2+} was predominant before the changing point of the discharge curve gradient (Figure 6b, /1d-1.54/). Upon discharge at 1.0 V, the spectrum comprised paramagnetic doublets indicating a mixture of 53% Fe^{3+}, 3% Fe^{2+}, and 38% Fe^0 (*IS* = 0.31, 1.03, and −0.01 mm/s, respectively), which suggested that the Fe^0-related reduction reaction was predominant after the changing point of the discharge curve gradient (Figure 6b, /1d-1.0/). After charging at 4.0 V, the spectrum comprised a mixture of 92% Fe^{3+} and 8% Fe^{2+} paramagnetic doublets, revealing that nearly all reduced iron species present after discharging returned to the trivalent state (Figure 6b, /1c-4.0/). These Mössbauer results indicate that on the Si-doped sample electrodes, the reduction of Fe^{3+} to Fe^{2+} reaction and Fe^0-generating conversion reaction were predominant until and below 1.6 V, respectively. Because of the formation of the Fe^0 doublet after discharge at 1.0 V, it is possible that Fe^0 could exist as ultrafine nanoparticles and/or a very complex coordination environment. Furthermore, the presence of a large quantity of Fe^{3+} and a minor amount of Fe^{2+} after discharging at 1.0 V suggests that the disproportion of the generated Fe^{2+} may have occurred ($3Fe^{2+} \Rightarrow 2Fe^{3+} + Fe^0$). Such a reaction has been reported to occur in nanosized α-Fe_2O_3,[7] suggesting that an analogous reaction occurred in the Si-doped samples. The capacity fading below 1.6 V with repeated cycling (Figures 4 and 5) may be because of the large valence state and volume changes related to the reaction of Fe^0. The conversion reaction of Fe^0 is well known, and conversion materials are generally regarded as high-capacity anode materials for Li-ion batteries. Thus, the Si-doped samples prepared in the present study have the potential for use as conversion anode materials. Further investigations are currently underway in our group.

Considering our previous report on the fast discharge/charge performance of the bacteriogenic iron-based oxide material in the voltage range of 1.5−4.0,[16] the two main explanations for why Si doping improved the electrochemical properties of the 2Fh materials should be as follows: (i) Si doping intrinsically changed the atomic arrangement of the 2Fh, leading to amorphous structure and formation of empty spaces suitable for the storage of Li ions, and (ii) the strong covalent Si−O bonds stabilized the 2Fh structure, enabling good cycle and rate performance. Further improvement of the electrochemical performance of this system should be possible by controlling the nanostructure (i.e., the porous structure and morphology) and selecting more appropriate doping elements. Investigation of the conversion reaction of Si-doped 2Fh materials is also an interesting topic for future consideration.

CONCLUSIONS

A bacteriogenic iron-based oxide material was a good model for creating new electrode materials. Si-doped 2Fh samples were prepared, and their Li storage properties were investigated in detail. The Si-doped samples have Si−O−Fe bonds with nanocrystalline structures for Si molar ratios less than 0.30 and an amorphous structure when the Si molar ratio becomes greater than 0.30. The samples comprised large agglomerates of strongly aggregated primary particles with diameters of ∼3 nm. Electrochemical discharge/charge measurements in the voltage range of 1.5−4.0 V revealed that the sample with $x = 0.30$ exhibited the most striking performance; the 20th discharge capacity was ∼100 mAh/g at a high current rate of 500 mA/g, which was four times higher than that of the Si-free sample and indicated large capacity and good rate and cycle performance. On the discharge curves for all Si-doped samples, the changing point for the discharge curve gradient was observed at ∼1.6 V. Ex-situ Mössbauer studies revealed that the reduction of Fe^{3+} to Fe^{2+} and Fe^0 conversion reaction were predominant before and after the changing point, respectively. This study clearly revealed that Si doping in the 2Fh structure intrinsically improved the Li storage properties of the 2Fh. Future research efforts will be directed at optimizing the doping elements, controlling the nanostructure, and hybridization of appropriate materials to achieve drastic enhancement of the performance of iron-based oxide materials.

ASSOCIATED CONTENT

Supporting Information

XRF data and Mössbauer parameters. The Supporting Information is available free of charge on the ACS Publications website at DOI: 10.1021/acs.inorgchem.5b01165.

AUTHOR INFORMATION

Corresponding Author

*Present address: Department of Applied Chemistry, School of Advanced Engineering, Kogakuin University, Hachioji 192-0015, Japan. Phone/fax: +81 426284537. E-mail: hideki-h@cc.kogakuin.ac.jp.

Notes

The authors declare no competing financial interest.

DOI: 10.1021/acs.inorgchem.5b01165
Inorg. Chem. 2015, 54, 7593−7599

■ ACKNOWLEDGMENTS

We thank Dr. S. Kohara, Dr. Y. Benino, and Mr. T. Maekawachi for helpful discussions. The synchrotron radiation experiments were performed at BL04B2 in SPring-8 (Proposal Nos. 2013A1098 and 2014B1558). This study was financially supported by the Special Funds for Education and Research from the Ministry of Education, Culture, Sports, Science and Technology and JSPS KAKENHI Grant Numbers 22860040, 24760550, and 23360309.

■ REFERENCES

(1) Zhu, G.-N.; Wang, Y.-G.; Xia, Y.-Y. *Energy Environ. Sci.* **2012**, *5*, 6652−6567.
(2) Wagemaker, M.; van Eck, E. R. H.; Kentgens, A. P. M.; Mulder, F. M. *J. Phys. Chem. B* **2009**, *113*, 224−230.
(3) Takai, S.; Kamata, M.; Fujine, S.; Yoneda, K.; Kanda, K.; Esaka, T. *Solid State Ionics* **1999**, *123*, 165−172.
(4) Komaba, S.; Suzuki, K.; Kumagai, N. *Electrochemistry* **2002**, *70*, 506−510.
(5) Jain, G.; Capozzi, C. J.; Xu, J. J. *J. Electrochem. Soc.* **2003**, *150*, A806−A810.
(6) Larcher, D.; Masquelier, C.; Bonnin, D.; Chabre, Y.; Masson, V.; Leriche, J. B.; Tarascon, J. M. *J. Electrochem. Soc.* **2003**, *150*, A133−A139.
(7) Larcher, D.; Bonnin, D.; Cortes, R.; Rivals, I.; Personnaz, L.; Tarascon, J. M. *J. Electrochem. Soc.* **2003**, *150*, A1643−A1650.
(8) Kanzaki, S.; Inada, T.; Matsumura, T.; Sonoyama, N.; Yamada, A.; Takano, M.; Kanno, R. *J. Power Sources* **2005**, *146*, 323−326.
(9) Komaba, S.; Mikumo, T.; Yabuuchi, N.; Ogata, A.; Yoshida, H.; Yamada, Y. *J. Electrochem. Soc.* **2010**, *157*, A60−A65.
(10) Komaba, S.; Mikumo, T.; Ogata, A. *Electrochem. Commun.* **2008**, *10*, 1276−1279.
(11) Hibino, M.; Terashima, J.; Yao, T. *J. Electrochem. Soc.* **2007**, *154*, A1107−A1111.
(12) Ghiorse, W. C. *Annu. Rev. Microbiol.* **1984**, *38*, 515−550.
(13) Emerson, D.; Fleming, E. J.; McBeth, J. M. *Annu. Rev. Microbiol.* **2010**, *64*, 561−583.
(14) Hashimoto, H.; Kobayashi, G.; Sakuma, R.; Fujii, T.; Hayashi, N.; Suzuki, T.; Kanno, R.; Takano, M.; Takada, J. *ACS Appl. Mater. Interfaces* **2014**, *6*, 5374−5378.
(15) Hashimoto, H.; Fujii, T.; Kohara, S.; Asaoka, H.; Kusano, Y.; Ikeda, Y.; Nakanishi, M.; Benino, Y.; Nanba, T.; Takada, J. *Mater. Chem. Phys.* **2012**, *137*, 571−575.
(16) Sakuma, R.; Hashimoto, H.; Kobayashi, G.; Fujii, T.; Nakanishi, M.; Kanno, R.; Takano, M.; Takada, J. *Mater. Lett.* **2015**, *139*, 414−417.
(17) Eggleton, R. A.; Fitzpatrick, R. W. *Clays Clay Miner.* **1988**, *36*, 111−124.
(18) Seehra, M.; Roy, P.; Raman, A.; Manivannan, A. *Solid State Commun.* **2004**, *130*, 597−601.
(19) Kohara, S.; Itou, M.; Suzuya, K.; Inamura, Y.; Sakurai, Y.; Ohishi, Y.; Takata, M. *J. Phys.: Condens. Matter* **2007**, *19*, 506101.
(20) Wright, A. C.; Hulme, R. A.; Grimley, D. I.; Sinclair, R. N.; Martin, S. W.; Price, D. L.; Galeener, F. L. *J. Non-Cryst. Solids* **1991**, *129*, 213−232.
(21) Jitianu, A.; Crisan, M.; Meghea, A.; Rau, I.; Zaharescu, M. *J. Mater. Chem.* **2002**, *12*, 1401−1407.
(22) Scarano, D.; Zecchina, A.; Bordiga, S.; Geobaldo, F.; Spoto, G.; Petrini, G.; Leofanti, G.; Padovan, M.; Tozzola, G. *J. Chem. Soc., Faraday Trans.* **1993**, *89*, 4123−4130.

DOI: 10.1021/acs.inorgchem.5b01165
Inorg. Chem. 2015, 54, 7593−7599